Author Manuscript
Accepted for publication in a peer-reviewed journal

NIST National Institute of Standards and Technology • U.S. Department of Commerce

Published in final edited form as:
Addit Manuf. 2019 December ; 30: . doi:10.1016/j.addma.2019.100844.

Part geometry and conduction-based laser power control for powder bed fusion additive manufacturing

Ho Yeung[*], **Brandon Lane**, **Jason Fox**
National Institute of Standards and Technology, Gaithersburg, MD, 20899, USA

Abstract

Laser powder bed fusion (LPBF) uses a focused, high power laser to repeatedly scan geometric patterns on thin layers of metal powder, which build up to a final, solid three-dimensional (3D) part. This process is somewhat limited in that the parts tend to have poorer surface finish (compared to machining or grinding) and distortion due to residual stress, as well as multiple other deficiencies. Typical laser scan strategies are relatively simple and use constant laser power levels. This elicits local variations in the melt pool size, shape, or temperature, particularly near sharp geometric features or overhang structures due to the relatively higher thermal conductivity of solid metal compared to metal powder. In this paper, we present a new laser power control algorithm, which scales the laser power to a value called the geometric conductance factor (GCF). The GCF is calculated based on the amount of solid vs. powder material near the melt pool. The algorithm for calculating GCF is presented along with some basic examples for clarification. Then, we detail the hardware and software implementation on the National Institute of Standards and Technology (NIST) additive manufacturing metrology testbed (AMMT), which includes co-axial melt pool monitoring using a high-speed camera. Six parts were fabricated out of nickel superalloy 625 (IN625) with the same nominal laser power, but with varying GCF algorithm parameters. We demonstrate the effect of tailored laser power on reducing the variability of melt pool intensity measured throughout the 3D build. Finally, we contrast the difference between the 'optimized' part vs. the standard build parameters, including the deflection of the final part top surface near the overhang and the variation of surface finish on the down-facing surfaces. Ultimately, the improvements to the in-situ process monitoring and part qualities demonstrate the utility and future potential tuning and optimizing more complex laser scan strategies.

Keywords

Additive manufacturing; Scan strategies; Laser power control; Overhanging structures

1. Introduction

Additive manufacturing (AM) of metal parts enables extended design flexibility, particularly for complex, freeform geometries. Out of the various metal AM processes, laser powder bed fusion (LPBF) provides superior part tolerance and surface finish quality under most circumstances. As such, metal parts fabricated using LPBF process are applied to multiple

[*]Corresponding author. ho.yeung@nist.gov (H. Yeung).

aerospace and medical part designs. Additionally, metal LPBF machine sales have increased exponentially in the last 8 years, and metal AM machine sales nearly doubled from 2016 to 2017 [1]. While geometric design flexibility is a key benefit of LPBF, there still exist certain constraints. Fine geometric features, such as sharp points, thin walls, small holes, etc., are inherently limited by the size scale of the metal powders (typically <50 μm). Overhang features, sometimes called down-facing or downskin surfaces, occur where the part surface forms some angle between the vertical build direction and horizontal plane, and the surface normal orients downward. Tolerance limits of both fine features and overhangs are additionally limited by phenomena associated with transient heat conduction, and its effect on melt pool shape, morphology, and stability.

One phenomenon that affects the overhang surface is ‘dross’, which is the formation of globular surface structures that degrade the surface finish. DePond et al. detailed the physical mechanisms that exacerbate dross formation [2], which they attribute to balling or capillary-driven melt pool instability, or partial sintering and adherence of powder to the surface. This results in poor shape tolerance or surface finish ([3,4]), and potentially causes build failure. For this reason, typical commercial AM preprocessing software identifies a ‘critical overhang angle’, above which either different parameters (e.g., upskin or downskin) or support structures are recommended. However, support structures need to be removed in post-processing, which elicits additional restrictions and manufacturing costs. Some studies have been developing methods to reduce support structure or ease their removal [5,6], or attempt support-free design [7].

AM powders, needing a sufficient volume to assume continuum properties, have much lower thermal conductivity than solids; potentially less than 1% that of solid material [8,9]). When the melt pool nears overhangs or fine features, the less conductive powder reduces heat conduction from the melt pool, creates overheating and melt pool instability, and increases melt pool size [10–13]). In turn, variation in melt pool geometry changes cooling rate and thermal gradients, contributing to microstructure heterogeneity [14] or variation in residual stress [15]. In addition to geometric effects, the laser scan path or scan strategy also contributes to the localized variation in cooling rates and thermal gradients.

Multiple works have investigated the effect of process parameters or scan strategy using commercial machines, or through multiphysics simulations. Determination of principal process parameters (scan speed, power, laser spot size, layer height) for full consolidation (e.g., near 100 % density) requires generally understood process mapping procedures [16–18]. Beyond this, a variety of experimental and modeling research has investigated the effect of scan strategy or geometric features such as overhangs on AM part qualities[1] :

- Part density or pore formation [19,20]
- Surface topology or surface structure [3,19,21,22]
- Residual stress, strain, or distortion [23–25]

[1]Some citations refer to other processes than LPBF, such as electron beam melting (EBM); however, the authors felt similarities in the research conclusions were analogous.

- Microstructure [26–30]

Little research in LPBF has attempted rectification of these effects, or locally tailoring scan path, velocity, or laser power to reduce defects or microstructure heterogeneity. Several authors have demonstrated that reducing laser power as the melt pool scans near overhangs can reduce dross and improve surface form and finish. Clijsters et al. [31] demonstrated a parameter adjustment algorithm that classifies different regions of a build layer based on the presence of surrounding solid or powder material, then changes the laser power within those regions. Mertens et al. [32] extended the algorithm to taper from low laser power at the overhang, to nominal power several layers up. Both studies demonstrated reduced dross formation. DePond et al. [2] followed suit by reducing laser power at an unsupported overhang, then intermittently increasing constant power setting with further layers. The laser power adjustment was guided by a-priori finite element simulation through a process co-authors dubbed “intelligent feed forward” or IFF [33], and allowed the authors to successfully fabricate a horizontal bridge structure over deep powder with minimal dross.

Although there are many examples of multiphysics AM simulations [34], there are few examples in research literature where LPBF scan parameters are adjusted based on a-priori simulation, or where reduced order models or empirical models are applied in real-time. One example of a-priori, model-based control was demonstrated with a surface-treating process called laser transformation hardening [35], which similarly to LPBF, scans a focused high power laser spot on a metal surface. In that paper, Martinez et al. incorporated a finite difference thermal simulation, described in Ukar et al. [36], in a real-time control loop using feedback from a pyrometer to reduce the variation in surface temperature. In an LPBF example, McMillan et al. reduced each layer in 3D part geometry to a 1-D finite difference heat transfer model [37]. Although, they did not control laser power based on a model in their experiments, they showed qualitative results comparable to the model prediction. Model-based control has been successfully demonstrated on directed energy deposition (DED) AM processes [38,39], which benefit from larger length scales and timescales required to resolve the physics of the process.

Similar to the reviewed research, the algorithm and experiments described in this paper demonstrate improvement in overhang surface finish by tailoring laser power based on a-priori calculated part geometry. Additionally, we demonstrate reduced melt pool variability throughout the part volume via observation by a high-speed camera. The laser power-scaling model and associated algorithm, called the geometric conductance factor (GCF), provides a framework for tailoring laser power based on the proportion of solid to powder material near the melt pool. It differs from previous work in the following ways:

1. The laser control algorithm is purely geometrically based. That is, it is not based on material properties or a heat transfer model, but on the relative ratio of solid to powder material near the melt pool.
2. The model takes the digital position and laser power commands as input, and adjusts the laser power for every scan position, which may vary the laser power within each scan line, and between each scan line.

3. Model parameters can be tuned empirically or through simulation, based on material choice or nominal build parameters
4. The algorithm time-steps through the scan process and is based on the solidification status of each voxel in each consecutive time-step, rather than utilizing the final build geometry.
5. The algorithm can potentially be applied in real time, within the LPBF controller architecture or as an aftermarket component, by intercepting the laser power and position digital command signal, building the GCF model, and adjusting the laser power command. The numerical methods are simple enough to realistically be applied at the typical LPBF controller clock frequency of 100 kHz.

2. Experimental methods

In LPBF AM processes, laser control is usually achieved through two digital commands: (1) Position command sent to the galvo controller to drive a pair of mirrors to direct the laser beam on an x–y plane. This can be denoted by a two-column array (XY), which represents a series of x–y coordinates. (2) Power command sent to the laser controller to adjust the laser beam power level. This can be denoted by a one-column array (L) of positive numbers. To fully synchronize the laser position and power, XY and L can be combined into a three-column array denoted by XYL. An example of XYL array is given in Fig. 1 (upper-left corner), which commands the laser moves from position (1, 5) to (5, 5) with constant power at 200 W. For the standard configuration, XYL is fed directly into the controller. However, the laser power can also be adjusted first to compensate, for example, the local conductance change. This is shown in Fig. 1 as an ‘alternative configuration’ (shaded region), where XYL is routed through a laser power adjustment module before being sent to the controller. L can be reduced as the scan approaches the overhanging edge, since the conductance decreases. A model is developed in this paper to quantify this conductance change, which the power adjustment can be based on.

2.1. Geometric conductance factor and laser power control

Similar to pixels in a bitmap, voxels represent values on a regular grid in three-dimensional (3D) space. The multilayer digital scan positions can be mapped into such a grid, with the corresponding laser power level as voxel value. Furthermore, if the heating laser is on, the voxel is labeled as ‘solidified’, similar to the concept of ‘element birth’ in finite element (FE) models [40]. The 3D structure can be reconstructed purely from the digital position and power commands (XYL). Once the structure is constructed, the relative conductance of each voxel can also be estimated based on the relative proportion of solid or powder material within each neighboring voxel. A Geometric Conductance Factor (GCF) can hence be assigned to each voxel. Laser power (or other parameters) can then be locally adjusted as a function of GCF at where shown by the “laser power adjustment” block in Fig. 1.

2.1.1. GCF and power control algorithm—The GCF model is represented as multilayer gray-scale 8-bit bitmaps stacked together, in-lieu of voxel representation, with the number of layers equal to the actual build. The GCF values are initialized to 0 for all pixels

for each layer, and then updated by iterating in time through the laser scan positions. If the laser power is never turned on over a pixel, it is considered never melted and consolidated, and GCF= 0. If it is the base layer (the build plate), GCF= 255. Otherwise, the GCF of a pixel will be assigned by:

$$\mathrm{GCF} = A + B \cdot \mathrm{GCF_b} + (1 - B) \cdot \mathrm{GCF_L} \quad (1)$$

where $A \in (0, 255)$, $B \in (0, 1)$. $\mathrm{GCF_b}$ is the GCF of the pixel directly below (on the layer immediately below), and $\mathrm{GCF_L}$ is the average GCF of each neighboring pixel in the same layer. A is related to the relative increase in local conductance due to the solidification, and B is a weight that scales the relative effect of GCF from the previous layer to the current layer. The maximum GCF is capped at 255. Once GCF is assigned to each pixel, laser power can be adjusted by:

$$\mathrm{L} = \mathrm{L_o}(C \cdot \mathrm{GCF_N} + (1 - C)) \quad (2)$$

where L is the adjusted laser power, $\mathrm{L_o}$ is the nominal power, $C \in [0, [1]]$ is a weight factor that limits the range the nominal power is varied, and $\mathrm{GCF_N}$ = GCF/255 is the normalized GCF value. Therefore, the model consists of three parameters, A, B, and C, which can be optimized experimentally, or through simulation.

The bitmap representation of the GCF is convenient to utilize the image processing tools or algorithms. The choice in pixel size creates a tradeoff between spatial resolution and computation time. The minimum pixel size is set based on the maximum interval between two digital XYL command positions, which depends on the digital rate and laser scan speed. For example, at 100 kHz digital rate and 1 m/s scanning speed, the interval (and minimum pixel size) will be 10 μm. One option for setting pixel/voxel size is to base it on the same relative scale as the melt-pool width. For the LPBF system and conditions described in this paper, this is assumed to be 100 μm.

2.1.2. Example GCF computational results—The implementation of the model is slightly more complicated than it appears to be, due to the recursive relationship of GCF and $\mathrm{GCF_L}$ in Eq. 1. An example is provided in Fig. 2 and explained below, where GCF values are updated for the first two points of a scan on the first powder layer ($\mathrm{GCF_b}$ = 255), and assumed parameters A = 4, B = 0.8.

When the first point (P1) is being scanned (Fig. 2a), $\mathrm{GCF_L}$ = 0 since all surrounding points are still powder. Plug in A = 4, B = 0.8, $\mathrm{GCF_b}$ = 255, and $\mathrm{GCF_L}$ = 0 into Eq. 1, GCF =4 + 0.8·255 +0.2·0 =208 for P1 (Eq. 1).

a. When the second point (P2) is being scanned, since P1 is solidified, $\mathrm{GCF_L} \neq 0$. Since the grid (pixel) size is selected to be the same as melt-pool size, $\mathrm{GCF_L}$ can be estimated by $\sum_1^{\mathrm{N}} \mathrm{GCF_1}/N$, where $\mathrm{GCF_i}$ is the i-th immediate neighbor. From Fig. 2b N = 8, hence $\mathrm{GCF_L}$ = 208/8 =26, and GCF =4 + 0.8·255 +0.2·26 = 213.2 for P2. However, this is only its initial value.

b. The solidification of P2 adds 213.2/N to the GCF_L at P1. This will increase the GCF at P1 by (1-B)·(213.2/N), or r·213.2 by putting

$$r = (1 - B)/N \tag{3}$$

Similarly, the increase of GCF at P1 by r·213.2 will in turn increase the GCF at P2 by (1-B)(r·213.2)/N, or r^2·213.2.

a. This recursive update process will iterate for infinite times. The i-th iteration will increase GCF by $r\text{^}\left(2^{i-1}\right) \cdot 213.2$ for P1, and $r\text{^}\left(2^{i}\right) \cdot 213.2$ for P2. That forms two geometric series:

$$S_{12} = \left(r + r^3 + r^5 \ldots\right) = \lim_{n \to \infty} r\left(1 - r^{2n}\right)/\left(1 - r^2\right) = r/\left(1 - r^2\right) \tag{4}$$

$$S_{21} = \left(r^2 + r^4 + r^6 \ldots .\right) = \lim_{n \to \infty} r^2\left(1 - r^{2n}\right)/\left(1 - r^2\right) = r^2/\left(1 - r^2\right) \tag{5}$$

plug in N = 8 and B = 0.8, r = 0.025, S_{12} = 0.025015 and S_{21} = 0.000625. The final GCF value will be 208 + S_{12}·213.2 = 213.33 for P1, and 213.2 + S_{21}·213.2 = 213.33 for P2. The subscript, for example in S_{12}, indicates the effect of P1 on P2.

When the scan finished at P2, the GCF values at P1 and P2 are the same. This is expected as two points should have no difference by the time P2 fully solidified. However, the GCF value used to adjust the laser power should be the one when the point is being scanned. In this case for P1 it is 208, for P2 it is 213.33. These are referred to as the dynamic GCF (values); and the final values (after all points were scanned within a layer) are referred to as the static GCF. The dynamic GCF is for laser power adjustment, the static GCF serves as GCF_b for the next layer. The dynamic GCF is scan sequence dependent, but the static GCF is not.

The example is continued in Fig. 3. When the third point (P3) is being scanned, it will affect not only P2, but also P1 (Fig. 3a). The initial GCF value of P3 = 4 +0.8·255 + 0.2·(213.33/8) = 213.33, but this value will have a recursive effect on both P2 and P1 as shown in the figure. Similar to S_{12} and S_{21} in Eqs. 4 and 5, the effect of P3 on P1 can be calculated by two geometric series:

$$S_{13} = r^2 + r^6 + r^{10} + \ldots.. = r^2/\left(1 - r^4\right) \tag{6}$$

$$S_{31} = r^4 + r^8 + r^{12} + \ldots . = r^4/\left(1 - r^4\right) \tag{7}$$

Therefore, each time a new point is scanned, all connected (directly or indirectly) points within the layer need to be updated. This update will quickly get very complicated, but also diminish quickly if r is small enough. For the sake of demonstration, only direct connected

points (immediate neighbors) will be updated in this example. Fig. 3a–c steps through the update sequence.

a. When the third point (P3) is scanned, GCF = (4 +0.8·255 + 0.2·(213.33/8)) ·(1 + 0.000625) =213.47; and GCF at P2 will be increased by 213.47 · 0.025015 = 5.34, to 218.67.

b. When fourth point (P4) is scanned, there are two solidified neighbors P2 and P3 (indicated by black circles in the Fig. 3b). GCF_l = (218.67 +213.47)/8 =54.02. GCF = (4 +0.8·255 +0.2·54.02)·(1 +0.000625·2) =219.07, GCF for P2 and P3 will be increased by 218.08·0.025016 = 5.46, to 224.15 and 218.94 respectively.

c. When fifth point (P5) is scanned, it has four neighbors, GCF_l = (213.33 +224.15 +218.94 + 219.07)/8 =109.44. Therefore GCF = (4 +0.8·255 + 0.2·109.44)·(1 +0.000625·3)= 230.32. GCF for P1 – P4 will be increased by, 230.32·0.025016 = 5.76.

The dynamic and static GCF values in the example are summarized in Table 1, as well as all intermediate values. The rows *t1* - *t5* represent the moment when points P1 – P5 are being scanned. The dynamic GCF of a point is its GCF value when it is being scanned, and is marked as italic in the table. As the scan continues, the dynamic GCF increases as it moves away from the edge/corner; If A is larger, this will increase faster. Therefore, A can be thought as a control for the '*edge*' effect. After the first layer, the GCF_b is no longer a constant. It is the static GCF of the previous layer. If B is larger, GCF of the current layer will be affected more by its previous layers, and hence B can be thought as a control for the '*bottom*' effect.

2.1.3. Software implementation of the GCF model—

In the software implementation of the GCF model, a slightly modified algorithm was used to balance the accuracy and computation time. In the previous example, only the immediate neighbors (one level) of the currently scanning point are updated. This might not be accurate enough when r (Eq. 3) is large (i.e., when B is small). The following algorithm was implemented which can update to any number of levels.

a. Three arrays were created. BA: array of binaries keeps track if a point is melted or not. GA: array of doubles keeps the dynamic GCF used for laser adjustment. VA: array of doubles keeps the intermediate GCF for computation.

b. A subset of VA is identified around the point being scanned (P) as M; M has $(2n+1)^2$-1 number of elements (points), where n is number of the update level defined.

c. The initial GCF value of P is set to the value recorded in array VA, and is used to update its neighbor, no matter if it is solidified or not. This update is similar to Fig. 3a but only in outward directions from P, and the updated values are stored in VA

d. M is mapped with BA to identify a subset S, which is the currently solidified points in M. The update in step c repeats for each point in S following a level by level sequence.

e. The GCF_L value of P is then evaluated based on VA; The GCF value of P is then calculated per Eq. 1 and updated into VA and GA.

f. Steps b to e are repeated for the next scan point.

The computation time will increase quickly with the number of levels. For the experiment detailed later, a three levels update was implemented. That is, $(2n+1)^2-1 = 48$ points are evaluated around the current scanned point. This gives a better approximation when B is small. However, the results of this study indicate that the model is more effective at a relatively larger B. A one level update may actually be sufficient for practical purposes. To further improve the computational efficiency, the number of scan points can be first reduced to match the pixel size. Laser power can be adjusted based on this reduced set of scan points and then interpolated back to the full set of the original digital commands. These steps can greatly improve computational efficiency.

2.2. Hardware and software integration

There is a lack of standard control protocols in LPBF AM systems, and the intermediate digital formats are not very well defined [41]. Nevertheless, most LPBF AM software starts with a 3D computer-aided design (CAD) file, and ends with the creation of digital position / power commands for galvo / laser control. One of the most commonly used digital communication protocols for galvo control is xy2–100, where the digital position commands are packaged into 20-bit packets and transmitted at 2 MHz clock rate to the galvo digital-to-analog receiver, converted to analog voltage to drive the galvo motor through a local proportional-integral-derivative (PID) loop. In other words, the xy2–100 commands are just a series of x–y positions similar to the XYL array in Fig. 1 but with a time step of 10 μs. Laser power on most commercial laser units can be controlled through an analog voltage input, where the digital power command can be transmitted and converted (D/A) in a similar way as galvo control signal. The digital position and power commands should exist in all LPBF AM systems in their simplest /raw format, irrespective of how the system is implemented. Even if the digital commands are not accessible as a digital file, they can be easily intercepted through the digital communication lines [42]. Hence an XYL array can always be created, and GCF power adjustment can be performed. Therefore, the GCF model can be integrated into virtually any LPBF AM systems.

Fig. 4 shows how the GCF module is integrated into the LPBF AM system developed at the National Institute of Standards and Technology (NIST). The system is divided into two parts: software and hardware. On the software side, the 3D CAD design is first sliced into 2D layers. Scan path and power are then generated based on the predefined scan strategy, and then interpolated into digital position and power commands. Normally these commands will be fed directly into the controller, but it can also be fed through a GCF module (dashed line rectangle in Fig. 4a) to have the laser power adjusted first. On the other hand, the controller will package the digital commands and transmit them to the laser system, based on the transmission protocol such as xy2–100. The transmission can be intercepted (at the red dashed line in Fig. 4b) and have GCF power adjustment in real-time. Since NIST developed the AM software in-house [43] and all digital files are readily accessible, the first approach was adapted in this study for its simplicity in implementation. As a proof of

concept for the second approach, the digital galvo position was successfully intercepted and decoded in real-time on a closed platform commercial machine.

2.3. Part and experiment design

2.3.1. Additive manufacturing metrology testbed (AMMT)—To utilize the GCF module in a full AM build, the Additive Manufacturing Metrology Testbed (AMMT) at NIST was used. The AMMT is a fully customized metrology instrument that enables flexible control and measurement of the LPBF process [44]. It incorporates a standard build bed, powder feed bed, and recoater arm found on most commercial LPBF systems. Since Fall of 2017, the AMMT also has an inert gas (typically Argon) recirculation and filtration system, and a laminar flow unit that blows and captures spatter or other ejecta from the build area.

As mentioned in the Introduction, one objective for controlling laser power during an AM build is to allow for more constant, unvarying melt pool size and/or intensity. Therefore, high-speed co-axial melt pool monitoring was employed on the AMMT, where a high-speed camera is optically aligned with the heating laser such that an image of the melt pool is maintained stationary within the camera's field of view (FoV). Fig. 5 shows a schematic of the co-axial monitoring configuration used in this study, and Table 2 provides salient characteristics of the imaging system.

Several pertinent features of the camera system are worth noting. Both the laser delivery and co-axial imaging optical paths pass through a linear translating z-lens (LTZ), which moves at high-speed based on the galvo X and Y position to ensure the laser and co-axial imager remain in focus on the build plane. This is used instead of the commonly used f-theta as these lenses incur chromatic aberrations, which may distort the co-axial melt pool images. The camera is a silicon-based complementary metal oxide semiconductor (CMOS) sensor with Cameralink-Full digital output to a peripheral component interconnect (PCI) based frame grabber card and stored on a hard drive. The camera can be set to trigger such that one frame is captured whenever it receives an external transistor-transistor logic (TTL) pulse. The AMMT controller allows for output of external triggers synchronized with the xy2–100 galvo and laser digital command mentioned in Section 2.2, and during the pre-processing steps, individual camera frame triggers can be selected at any point within the 3D part. Therefore, melt pool images of only the areas and points within a build layer of interest are collected, and others (e.g., when the laser is off) can be ignored. This is limited by either the acquisition rate of the camera hardware (< 10 000 frames/s in this paper), or the digital command rate (100 kHz). Additionally, the physical position of each camera frame trigger can be mapped back to the physical location within the part. The camera trigger scheme and image processing for this experiment are described in Section 3.1.

2.3.2. Parts design, parameter selection, and material—Overhanging structure is identified to study the effectiveness of the GCF based power control. A part is designed with a series of downward facing wedges of angles 45, 60, 75 and 90 degrees (Fig. 6). Nickel alloy 625 (IN625) powder is used, with particle size distribution of D_{10} = 16.4 μm, D_{50} =30.6 μm, and D_{90} =47.5 μm. The build plates are 12.5 mm thick IN625, and the AMMT

chamber is purged and backfilled with Argon to obtain an oxygen level less than 705 mg/m^3. The laminar flow unit is used, with flow rate of 300 L/min, although the flow velocity above the build is unknown at this time. Nominal scan parameters for IN625 are based on a commercial LPBF system. Scan speed is 800 mm/s, laser power 195 W, interlayer rotation 67°, hatch spacing 100 μm, and layer thickness 20 μm. The part has a height of 10 mm, which is equivalent to 500 layers. The build file (multilayer digital scan position and power commands) was first created using standard parameters to act as the base configuration, and then processed with GCF model with five different combinations of A and B parameters, while C was kept constant at 0.25. Therefore, six parts (configurations) were created in total, with part 1 as the base configuration.

Fig. 7 shows the GCF models for part 2–6. The experiment is designed to compare the edge effect and bottom effect; hence combinations of small and large A and B values were selected. Note the variation of the color (seen in online version of this paper), which represents the GCF value, around the edge and overhanging region in each model. Comparing model 2 and 3, both have strong edge effect due to a small A value. However, the much larger B value for model 3 gives it more ‘blue’ in color (smaller GCF) at the overhang. Comparing model 5 and 6, both have a smaller edge effect due to a larger A value. However, the larger B value in model 6 made the edge effect even less obvious. Model 4 has medium A and B values, hence a balanced edge and bottom effect are shown.

The six parts were positioned carefully on the build plate to allow enough gaps between each part, and the overhanging edge is protected from the recoating direction. Fig. 8a shows the layout, with the color indicating power variations. The laser power is adjusted based on the dynamic GCF values in Fig. 7, with a constant C =0.25 for Eq. 2. Fig. 8b shows the enlarged view of the laser power changes at the 45° overhangs. Note the gradual variation of laser power within a scan line when approaching the overhangs and edges. An expanded view of the region marked by the dotted rectangle is also shown in Fig. 8c, which exemplifies variation of power within and between each scan line

2.3.3. Surface roughness measurement—Surface height data was acquired with an Alicona^2 focus variation (FV) system [45]. All measurements were performed using a 20x objective lens with a 0.4 numerical aperture, creating scans with lateral point spacing of 0.44 μm in both x and y directions and 806.4 μm × 806.4 μm field of view (FoV). Larger FoVs were created by stitching multiple scans together with approximately 11% overlap. Stitching was performed by the manufacturer’s proprietary algorithms. Coaxial and off-axis (ring) light was used and light settings were adjusted to minimize data dropout for each scan. Height data was transferred to commercially available software (MATLAB and DigitalSurf’s ConfoMap) for quantitative analysis.

3. Experiment results and discussion

All six parts were built successfully. The building process was in-situ monitored using a high-speed co-axial camera (section 2.3.1). The images were analyzed to identify possible relationships between the melt-pool properties and GCF parameters. Parts were cut off from

the base plate by electrical discharge machining (EDM) and examined under optical microscope. Parts 1 and 3 were also scanned with the FV system for surface roughness.

3.1. Melt pool imaging results

The in-situ melt-pool images were captured by triggering the camera at designated positions (Section 2.3.1). The images were saved as 8-bit grayscale bitmaps and processed to determine the melt-pool intensity [46], which was used as the indication of the effectiveness of power adjustment by the GCF model. The total integrated camera signal is calculated by averaging the gray scale values of all pixels in the image. The camera integration time was set to 20 μs, such as there was no saturation in the images. This ensures that the total integrated camera signal is a meaningful representation of the melt-pool intensity [47], and this signal is referred to as melt-pool image intensity. The image is synchronized with position, and the image intensity is also plotted together with the laser power and speed in Fig. 9.

The camera was triggered in such a way that for each layer one of the 45° overhangs would be imaged at 10 000 frames per second, hence the same part was imaged once per six layers or 83 times total. This ensured the sample base is big enough for statistical analysis. A total of 5 251 145 images were taken and processed, and the results are summarized in Fig. 10. One interesting observation from Fig. 10a is, while part 3 has the largest variation in the laser power (because the GCF adjustment), it has the smallest variation (σ) in the melt-pool image intensity. Fig. 10b plots σ in A–B parameter space of the GCF model; the trend of increasing B while decreasing σ is obvious. If the goal is to keep the melt-pool intensity consistent, the GCF model can be optimized to achieve that.

3.2. Visual part inspection

Fig. 11a shows the six parts attached to the base plate as built, and Fig. 11b–d show different views of the 45° overhangs. It appears that part 3 has the best quality of the overhang edges (red arrows). This is particularly obvious from the side view (Fig. 11d) while comparing with the scorched rough edges of the other parts. This is also consistent with the in-situ melt-pool monitoring results shown in Fig. 10, where part 3 has the minimum variation in melt-pool image intensity.

3.3. Surface topography

To determine the improvement due to the GCF algorithm, surface topography of the upward-facing and downward-facing surfaces for part 1 and part 3 are analyzed and compared. A focus variation system (Section 2.3.3) was used to measure the “height” of the surfaces. Fig. 12 shows the comparison of the upward-facing surfaces and Fig. 13 shows the comparison of the downward-facing surfaces. Height data presented in Figs. 12 and 13 has been leveled by subtracting a best-fit plane from the data. Histograms of the height data are presented in Figs. 12(c) and 13 (c). Additionally, the histograms have been fitted with a normal gaussian distribution and shown as a red line in Figs. 12(c) and 13 (c) for comparison.

For the comparison of the upward-facing surfaces in Fig. 12, lower variations in height can be seen in Fig. 12(b) near the downward-facing edge (i.e., in the values near x = 5500 μm),

suggesting a more stable and consistent melt pool size and shape near the downward facing edge. This theory is also supported by the histograms in Fig. 12(c), which show a shorter and wider distribution in part 1 versus part 3. Additionally, part 1 shows more values at the highest points of the distribution than part 3, which is highlighted by the red arrows in Fig. 12(c).

For the comparison of downward-facing surfaces in Fig. 13, the surfaces are very similar qualitatively; however, fewer values in the highest height range (i.e., z values of 150 μm to 300 μm) can be seen in the surface near the top of the build (i.e., in the values from x = 6000 μm to x = 8000 μm). Part 1 also shows a slightly shorter and wider distribution of heights in Fig. 13(c), although it is not as pronounced as the upward-facing surfaces, and more values at the highest points of the distributions, which is highlighted by the red arrows in Fig. 13(c).

In addition to the height distributions shown in the previous figures, average height values as a function of proximity to an edge are compared as this is where the GCF algorithm should have the most significant impacts to surface topography. For these comparisons, x and y positions are consistent with positions defined in Fig. 12 for the upward-facing surfaces and Fig. 13 for the downward-facing surfaces. To better show the impact of the GCF near the edge, a best-fit plane is found for the z values in the range of 0 μm ≤ x ≤ 4500 μm and 1000 μm ≤ y ≤ 5000 μm and subtracted from all z values in the dataset for the upward-facing surfaces. For downward-facing surfaces, a best-fit plane is found for the z values in the range of 2400 μm ≤ x ≤ 4900 μm and 1500 μm ≤ y ≤ 4500 μm and subtracted from all z values in the dataset.

Fig. 14 shows the average height of the upward-facing surfaces for part 1 and part 3 as a function of position along the x-direction. The average height calculation is limited to values of y ≥ 1000 μm and y ≤ 5000 μm to prevent the influence of the vertical edges of the part in the analysis. In this figure, average height values approaching x =6000 μm are akin to approaching the downward-facing edge of the part and a statistically significant decrease in the height near the downward-facing edge of part 3 can be seen. It is theorized that this decrease in height is due to either a reduced consolidation of material and/or reduced residual stress, which would cause the part to curl up to higher values of z, from a more consistent melt pool size and shape near the downward-facing edge. Either of which would support the hypothesis that the GCF algorithm is improving part quality.

Similar analysis was performed for the downward-facing surfaces shown in Fig. 15. As previously mentioned, a best-fit plane is found for the z values in the range of 2400 μm ≤ x ≤ 4900 μm and 1500 μm ≤ y ≤ 4500 μm and subtracted from all z values in the dataset. As with the upward-facing surface analysis, approaching values of x =6000 μm in Fig. 15 are akin to approaching the upward-facing surface of the part. Average values in Fig. 15 are limited to values where y ≥ 1500 μm and y ≤ 4500 μm to prevent influence from the vertical edges of the part in the analysis. In Fig. 15, there is a larger standard deviation in the datasets due to the larger variation in height of downward-facing surfaces compared to upward-facing surfaces [48] and little difference between part 1 and part 3 can be seen.

While it was expected that the implementation of the GCF would improve part quality of the downward facing surfaces, particularly as we explore the data in Fig. 15, there is a lack of statistical difference between the two parts. This may be due to competing factors. It was expected that reductions in over-melting and variation of surface height (seen in Fig. 13) would create statistically significant differences in Fig. 15. This lack of difference, however, could be attributed to reductions in residual stress, which was previously mentioned as a reason for the differences seen in Fig. 14. Since Fig. 15 is showing the downward facing surfaces, increases in over-melting will create higher values of z and increases in residual stress will create smaller values of z in our dataset.

Thus, to further investigate the improvement in part quality due to the GCF, the arithmetic mean of the surface (Sa) and the root mean square height of the surface (Sq) as defined by ISO 25,178 [49] are calculated using the commercially available ConfoMap software. For this analysis, a 2.24 mm by 2.24 mm patch of the surfaces (3 × 3 FoV stitched measurement) was transferred to the software and leveled by subtracting a least square fit plane from the surfaces prior to calculation. By performing the analysis on a small area, the influence of residual stress hypothesized to be influencing data in Fig. 15 should be reduced. As expected, reductions in the unfiltered surface texture parameters Sa and Sq due to the implementation of the GCF can be seen in Fig. 16. Additionally, a digital gaussian filter as defined by ISO 16,610 [50] with a cut-off wavelength of 0.08 mm is applied to the surfaces separating the surface by waviness and roughness, which are the long and short spatial wavelengths, respectively. From this result we can see that the waviness (i.e., the longer spatial wavelengths) of the surface are contributing more to the reduction and surface texture parameters than the shorter spatial wavelengths. This also suggests that the reduction in surface texture is due to a more consistent melt pool depth, width, and length, whose measurements are on the order of hundreds of micrometers to millimeters, as opposed to the attachment of partially melted powder particles, whose diameters are on the order of tens of micrometers.

The surface topography shows a clear improvement in the downward-facing surface roughness for the part built with GCF adjustment (Fig. 16). While the upward-facing surface roughness is not significantly different since the self-recovery process of adding layers, the much higher warp at the edge for the part built without GCF shows the larger residual stress resulted from excessive heat (Fig. 15), which is exactly what the GCF compensates for.

4. Conclusions and discussion

This paper detailed a method and algorithm for controlling laser power in an LPBF process based on locally varying relative proportion of solid or powder material. A factor called the Geometric Conductance Factor (GCF) is calculated, and laser power is linearly scaled to the GCF throughout the build, which effectively reduces the power near part edges or overhangs. An overhanging structure was built as a demonstration. However, GCF can be applied to different geometries such as thin wall or lattice structures. The principle is the same, to compensate for the conductivity difference by adjusting the laser power.

This algorithm was implemented on the controller of the NIST Additive Manufacturing Metrology Testbed. To test the algorithm, six parts were designed with varying overhang geometry and varying GCF parameters to test the effect on in-situ melt pool intensity measured via high-speed camera configured for co-axial melt pool monitoring. One of the parts (Part 1) used constant power level and nominal process parameters.

In-situ measurements showed that the GCF parameters that enabled more extreme reduction in laser power and most varied and controlled laser power during the build also resulted in the lowest measured melt pool intensity variation. Part 3, which had GCF parameters that created the most extreme power control, additionally showed reduced scorching on the downfacing overhang surface and was selected for more detailed comparison to Part 1. Part 3 showed reduced elevation on the edge of the top, upward facing surface. Average and standard deviation of surface profile height on the down-facing surfaces showed little difference; however, there was measurable reduction in areal surface texture parameters. These factors are all consistent with the theory that controlled reduction of laser power near edges and overhangs contributed to a more consistent and uniform melt pool.

Overall, the experiment parameters and laser power settings selected in this study were relatively conservative to ensure all parts were printed successfully. However, results showed the part with the most highly varied and controlled laser power resulted in the most improvement in the measured part qualities. Therefore, while improvements were demonstrated, an ‘optimum’ set of model parameters was not conclusively determined. Nevertheless, the utility of this laser control algorithm was successfully demonstrated, and future research will utilize a combined simulation and experimental approach to determine true optimal GCF parameters. In addition, the effect on part qualities such as internal residual stress, microstructure heterogeneity, and concentration of pore or void defects will be studied.

References

[1]. Wohlers T, Wohler’s Report 2017: 3D Printing and Additive Manufacturing State of the Industry, Fort Collins, CO, (2017).

[2]. DePond PJ, Guss G, Ly S, Calta NP, Deane D, Khairallah S, Matthews MJ, In situ measurements of layer roughness during laser powder bed fusion additive manufacturing using low coherence scanning interferometry, Mater. Des. 154 (2018) 347–359, 10.1016/j.matdes.2018.05.050.

[3]. Fox JC, Moylan SP, Lane BM, Effect of process parameters on the surface roughness of overhanging structures in laser powder bed fusion additive manufacturing, Procedia Cirp 45 (2016) 131–134.

[4]. Wang D, Yang Y, Yi Z, Su X, Research on the fabricating quality optimization of the overhanging surface in SLM process, Int. J. Adv. Manuf. Technol. 65 (2013) 1471–1484, 10.1007/s00170-012-4271-4.

[5]. Calignano F, Design optimization of supports for overhanging structures in aluminum and titanium alloys by selective laser melting, Mater. Des. 64 (2014) 203–213, 10.1016/j.matdes.2014.07.043.

[6]. Cheng B, Chou K, Geometric consideration of support structures in part overhang fabrications by electron beam additive manufacturing, Comput.-Aided Des. 69 (2015) 102–111, 10.1016/j.cad.2015.06.007.

[7]. Leary M, Merli L, Torti F, Mazur M, Brandt M, Optimal topology for additive manufacture: a method for enabling additive manufacture of support-free optimal structures, Mater. Des. 63 (2014) 678–690, 10.1016/j.matdes.2014.06.015.

[8]. Alkahari MR, Furumoto T, Ueda T, Hosokawa A, Tanaka R, Abdul Aziz MS, Thermal conductivity of metal powder and consolidated material fabricated via selective laser melting, Key Eng. Mater. 523–524 (2012) 244–249 doi:10.4028/www.scientific.net/KEM.523-524.244.

[9]. Wei LC, Ehrlich LE, Powell-Palm MJ, Montgomery C, Beuth J, Malen JA, Thermal conductivity of metal powders for powder bed additive manufacturing, Addit. Manuf. 21 (2018) 201–208, 10.1016/j.addma.2018.02.002.

[10]. Craeghs T, Clijsters S, Yasa E, Bechmann F, Berumen S, Kruth J-P, Determination of geometrical factors in Layerwise Laser melting using optical process monitoring, Opt. Lasers Eng. 49 (2011) 1440–1446, 10.1016/j.optlaseng.2011.06.016.

[11]. Craeghs T, Clijsters S, Kruth J-P, Bechmann F, Ebert M-C, Detection of process failures in layerwise laser melting with optical process monitoring, Phys. Procedia 39 (2012) 753–759, 10.1016/j.phpro.2012.10.097.

[12]. Heigel J, Whitenton EP, Measurement of thermal processing variability in powder bed fusion, Proc. 2018 ASPE Euspen Summer Top. Meet. - Adv. Precis. Addit. Manuf. (2018).

[13]. Lane B, Whitenton E, Moylan S, Multiple sensor detection of process phenomena in laser powder bed fusion, Proc. SPIE (2016), 10.1117/12.2224390 pp. 986104–986104–9.

[14]. Kok Y, Tan XP, Wang P, Nai MLS, Loh NH, Liu E, Tor SB, Anisotropy and heterogeneity of microstructure and mechanical properties in metal additive manufacturing: a critical review, Mater. Des. 139 (2018) 565–586, 10.1016/j.matdes.2017.11.021.

[15]. Strantza M, Ganeriwala RK, Clausen B, Phan TQ, Levine LE, Pagan D, King WE, Hodge NE, Brown DW, Coupled experimental and computational study of residual stresses in additively manufactured Ti-6Al-4V components, Mater. Lett. 231 (2018) 221–224, 10.1016/j.matlet.2018.07.141.

[16]. Beuth J, Klingbeil N, The role of process variables in laser-based direct metal solid freeform fabrication, JOM. 53 (2001) 36–39.

[17]. Yadroitsev I, Smurov I, Selective laser melting technology: From the single laser melted track stability to 3D parts of complex shape, Phys. Procedia (2010) 551–560, 10.1016/j.phpro.2010.08.083.

[18]. Yadroitsev I, Krakhmalev P, Yadroitsava I, Hierarchical design principles of selective laser melting for high quality metallic objects, Addit. Manuf. 7 (2015) 45–56.

[19]. Rashid R, Masood SH, Ruan D, Palanisamy S, Rahman Rashid RA, Brandt M, Effect of scan strategy on density and metallurgical properties of 17–4PH parts printed by Selective Laser Melting (SLM), J. Mater. Process. Technol. 249 (2017) 502–511, 10.1016/j.jmatprotec.2017.06.023.

[20]. Tammas-Williams S, Zhao H, Léonard F, Derguti F, Todd I, Prangnell PB, XCT analysis of the influence of melt strategies on defect population in Ti–6Al–4V components manufactured by Selective Electron beam Melting, Mater. Charact. 102 (2015) 47–61, 10.1016/j.matchar.2015.02.008.

[21]. Chen H, Gu D, Xiong J, Xia M, Improving additive manufacturing processability of hard-to-process overhanging structure by selective laser melting, J. Mater. Process. Technol. 250 (2017) 99–108, 10.1016/j.jmatprotec.2017.06.044.

[22]. Triantaphyllou A, Giusca CL, Macaulay GD, Roerig F, Hoebel M, Leach RK, Tomita B, Milne KA, Surface texture measurement for additive manufacturing, Surf. Topogr. Metrol. Prop. 3 (2015) 24002, 10.1088/2051-672X/3/2/024002.

[23]. Bagg SD, Sochalski-Kolbus LM, Bunn JR, Raleigh NC, United StatesThe Effect of Laser Scan Strategy on Distortion and Residual Stresses of Arches Made With Selective Laser Melting2016, The Effect of Laser Scan Strategy on Distortion and Residual Stresses of Arches Made With Selective Laser Melting (2016), https://ntrs.nasa.gov/search.jsp?R=20160008858.

[24]. Cheng B, Shrestha S, Chou K, Stress and deformation evaluations of scanning strategy effect in selective laser melting, Addit. Manuf. In Press-Corrected Proof (2016), 10.1016/j.addma.2016.05.007.

[25]. Dai K, Shaw L, Distortion minimization of laser-processed components through control of laser scanning patterns, Rapid Prototyp. J. 8 (2002) 270–276.

[26]. Dehoff RR, Kirka MM, Sames WJ, Bilheux H, Tremsin AS, Lowe LE, Babu SS, Site specific control of crystallographic grain orientation through electron beam additive manufacturing, Mater. Sci. Technol. 31 (2015) 931–938, 10.1179/1743284714Y.0000000734.

[27]. Geiger F, Kunze K, Etter T, Tailoring the texture of IN738LC processed by selective laser melting (SLM) by specific scanning strategies, Mater. Sci. Eng. A. 661 (2016) 240–246, 10.1016/j.msea.2016.03.036.

[28]. Lee YS, Kirka MM, Dinwiddie RB, Raghavan N, Turner J, Dehoff RR, Babu SS, Role of scan strategies on thermal gradient and solidification rate in electron beam powder bed fusion, Addit. Manuf. 22 (2018) 516–527, 10.1016/j.addma.2018.04.038.

[29]. Liu J, Zhou Y, Fan Y, Chen X, Effect of laser hatch style on densification behavior, microstructure, and tribological performance of aluminum alloys by selective laser melting, J. Mater. Res. 33 (2018) 1713–1722, 10.1557/jmr.2018.166.

[30]. Raghavan N, Simunovic S, Dehoff R, Plotkowski A, Turner J, Kirka M, Babu S, Localized melt-scan strategy for site specific control of grain size and primary dendrite arm spacing in electron beam additive manufacturing, Acta Mater. 140 (2017) 375–387, 10.1016/j.actamat.2017.08.038.

[31]. Clijsters S, Craeghs T, Kruth J-P, A priori process parameter adjustment for SLM process optimization, Innov. Dev. Virtual Phys. Prototyp. (2011) 553–560, 10.1201/b11341-89 (Accessed September 22, 2015).

[32]. Mertens R, Clijsters S, Kempen K, Kruth J-P, Optimization of scan strategies in selective laser melting of aluminum parts with downfacing areas, J. Manuf. Sci. Eng. 136 (2014), 10.1115/1.4028620 061012–061012.

[33]. Matthews MJ, Intelligent Feed Forward (n.d.). https://acamm.llnl.gov/models/intelligent-feed-forward (Accessed August 31, 2018), (2019).

[34]. Markl M, Koerner C, Multiscale modeling of powder bed-based additive manufacturing, in: Clarke DR (Ed.), Annual Review of Materials Research, Vol. 46 2016, pp. 93–123. Annual Reviews, Palo Alto.

[35]. Martínez S, Lamikiz A, Ukar E, Tabernero I, Arrizubieta I, Control loop tuning by thermal simulation applied to the laser transformation hardening with scanning optics process, Appl. Therm. Eng. 98 (2016) 49–60, 10.1016/j.applthermaleng.2015.12.037.

[36]. Ukar E, Lamikiz A, López de Lacalle LN, Martinez S, Liébana F, Tabernero, Thermal model with phase change for process parameter determination in laser surface processing, Phys. Procedia 5 (2010) 395–403, 10.1016/j.phpro.2010.08.066.

[37]. McMillan M, Leary M, Brandt M, Computationally efficient finite difference method for metal additive manufacturing: a reduced-order DFAM tool applied to SLM, Mater. Des. 132 (2017) 226–243, 10.1016/j.matdes.2017.06.058.

[38]. Devesse W, De Baere D, Guillaume P, Design of a model-based controller with temperature feedback for laser cladding, Phys. Procedia 56 (2014) 211–219, 10.1016/j.phpro.2014.08.165.

[39]. Li J, Wang Q, Michaleris P. (Pan), Reutzel EW, Nassar AR, An extended lumped-parameter model of melt–Pool geometry to predict part height for directed energy deposition, J. Manuf. Sci. Eng. 139 (2017), 10.1115/1.4037235 91016–91016–14.

[40]. Schoinochoritis B, Chantzis D, Salonitis K, Simulation of metallic powder bed additive manufacturing processes with the finite element method: a critical review, Proc. Inst. Mech. Eng. Part B J. Eng. Manuf. 231 (2017) 96–117.

[41]. Nassar AR, Reutzel EW, A proposed digital thread for additive manufacturing, Proc. Solid Free. Fabr. Symp. (2013) 19–25.

[42]. Dunbar AJ, Nassar AR, Reutzel EW, Blecher JJ, A real-time communication architecture for metal powder bed fusion additive manufacturing, Proc. Solid Free. Fabr. Symp. (2016) 67–80.

[43]. Yeung H, Lane BM, Donmez MA, Fox JC, Neira J, Implementation of advanced laser control strategies for powder bed fusion systems, Procedia Manuf. (2018) 871–879, 10.1016/j.promfg.2018.07.112.

[44]. Lane B, Mekhontsev S, Grantham S, Vlasea M, Whiting J, Yeung H, Fox J, Zarobila C, Neira J, McGlauflin M, Hanssen L, Moylan S, Donmez MA, Rice J, Design, developments, and results from the nist additive manufacturing metrology testbed (ammt), Proc. 26th Annu. Int. Solid Free. Fabr. Symp. (2016) 1145–1160.

[45]. ISO 25178–251782606, Geometrical Product Specification (GPS) – Surface Texture: Areal – Part 606: Nominal Characteristics of Non-contact (focus Variation) Instruments, (2015), p. 2015 (Accessed October 12, 2018), https://www.iso.org/standard/59716.html.

[46]. Yeung H, Lane B, Fox J, Kim F, Heigel J, Neira J, Continuous laser scan strategy for faster build speeds in laser powder bed fusion system, Proc. Solid Free. Fabr. Symp. (2017) 1423–1431.

[47]. Fisher BA, Lane B, Yeung H, Beuth J, Toward determining melt pool quality metrics via coaxial monitoring in laser powder bed fusion, Manuf. Lett. 15 (2018) 119–121, 10.1016/j.mfglet.2018.02.009. [PubMed: 29888171]

[48]. Fox JC, Moylan S, Lane BM, Preliminary study toward surface texture as a process signature in laser powder bed fusion additive manufacturing, Proc. 2016 ASPE Summer Top. Meet. Dimens. Accuracy Surf. Finish Addit. Manuf. (2016) (Accessed April 6, 2017), https://www.nist.gov/publications/preliminary-study-toward-surface-texture-process-signature-laser-powder-bed-fusion.

[49]. ISO 25178–2:2012, Geometrical Product Specifications (GPS) - Surface Texture: Areal - Part 2: Terms, Definitions, and Surface Texture Parameters, ISO, Geneva, 2012.

[50]. ISO 16610–21:2011, Geometrical Product Specifications (GPS) – Filtration – Part 21: Linear Profile Filters: Gaussian Filters, ISO, Geneva, 2011.

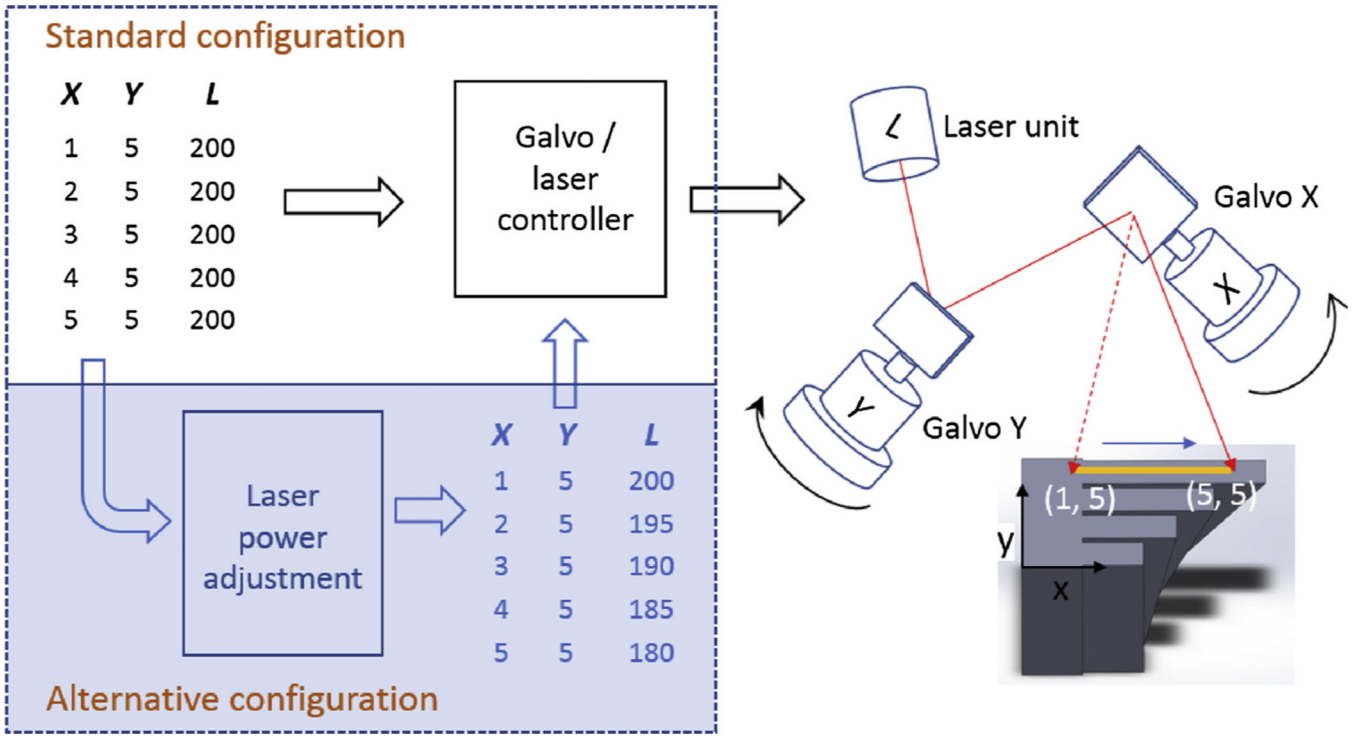

Fig. 1.

LPBF laser control. XYL array is the digital commands for galvo position (XY) and laser power (L). Sample values are assigned to L to demonstrate how the laser power can be adjusted. Typical units for position (XY) are millimeters, and laser power is Watts.

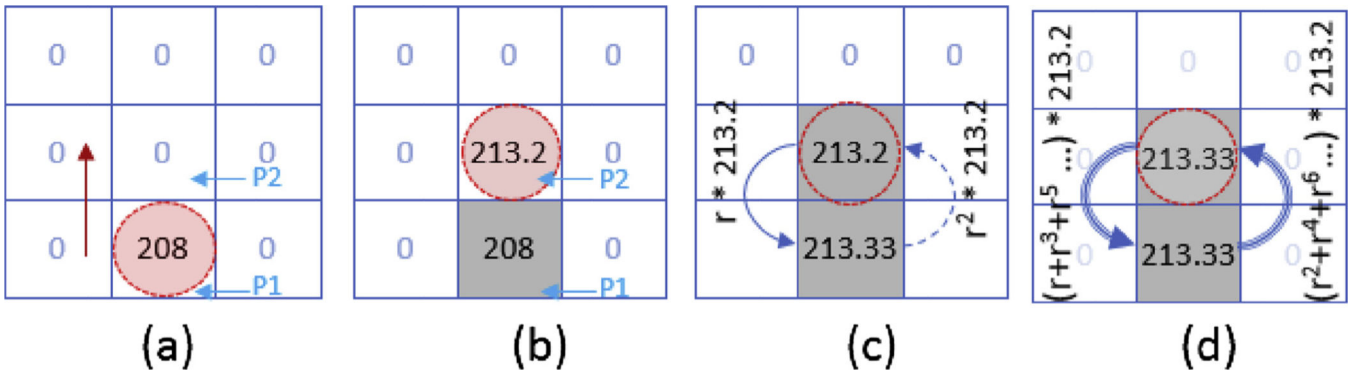

Fig. 2.

GCF update example. The number in the grid indicates its current GCF value. The circle indicates the current laser position. The shaded circle indicates the instant when the melting just starts. P1 and P2 marked the first two scan points, (a) – (d) show how the GCF values change for P1 and P2 as the scan proceeds.

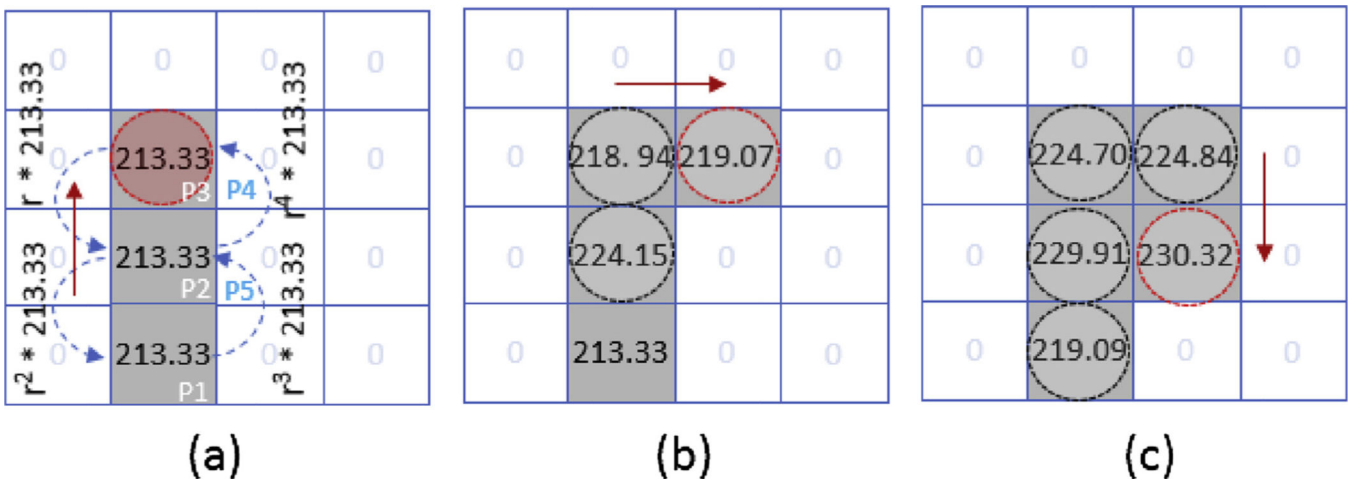

Fig. 3.

GCF update example continued. (a) – (c) show how the GCF value changes for each point as the scan proceeds from point P3 to P5.

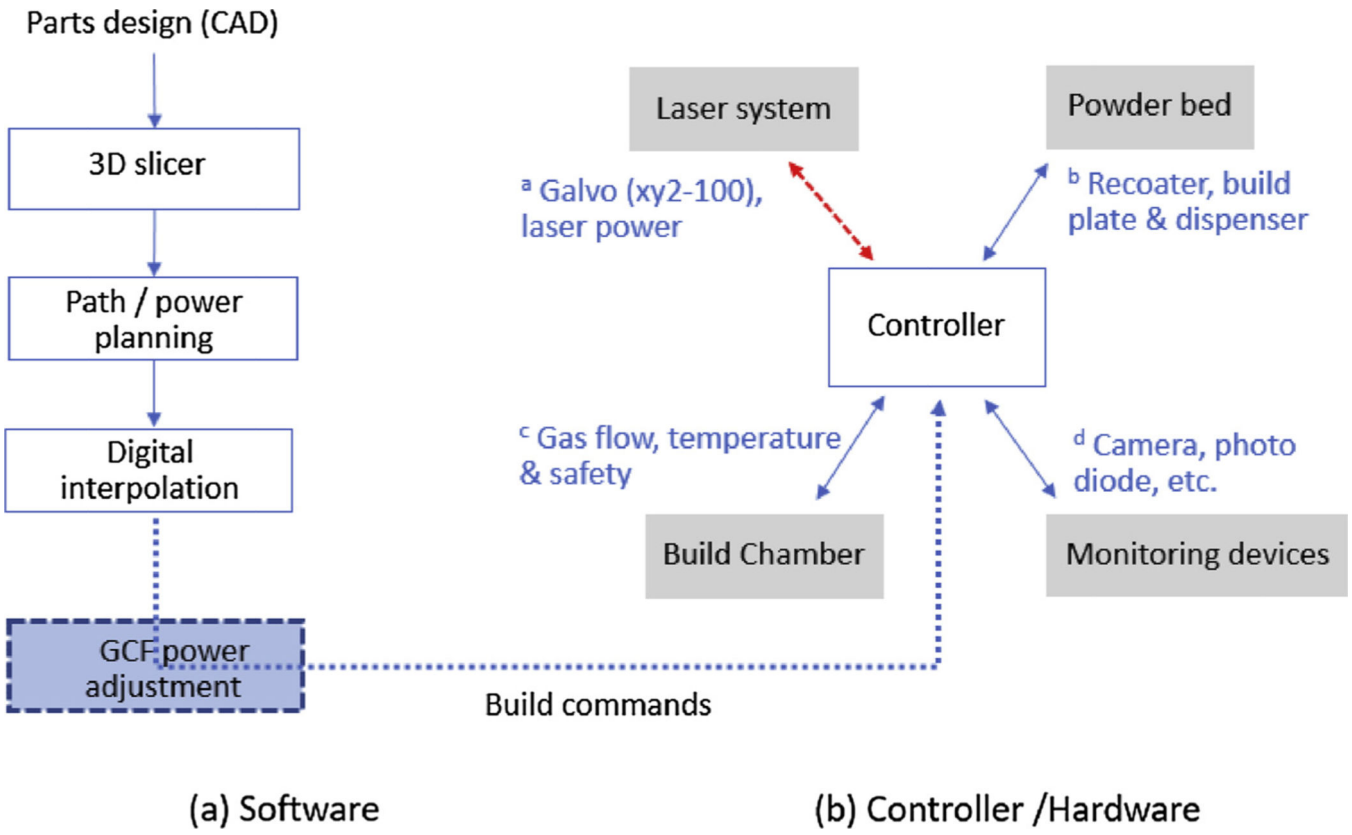

Fig. 4.

Integration of GCF model into NIST Additive Manufacturing Metrology Testbed. (For interpretation of the references to colour in this figure text, the reader is referred to the web version of this article).

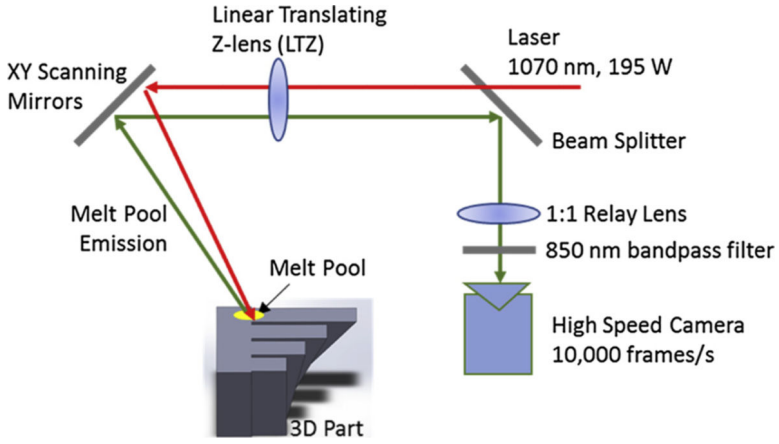

Fig. 5.

Schematic of laser delivery and co-axial melt pool monitoring system on the AMMT.

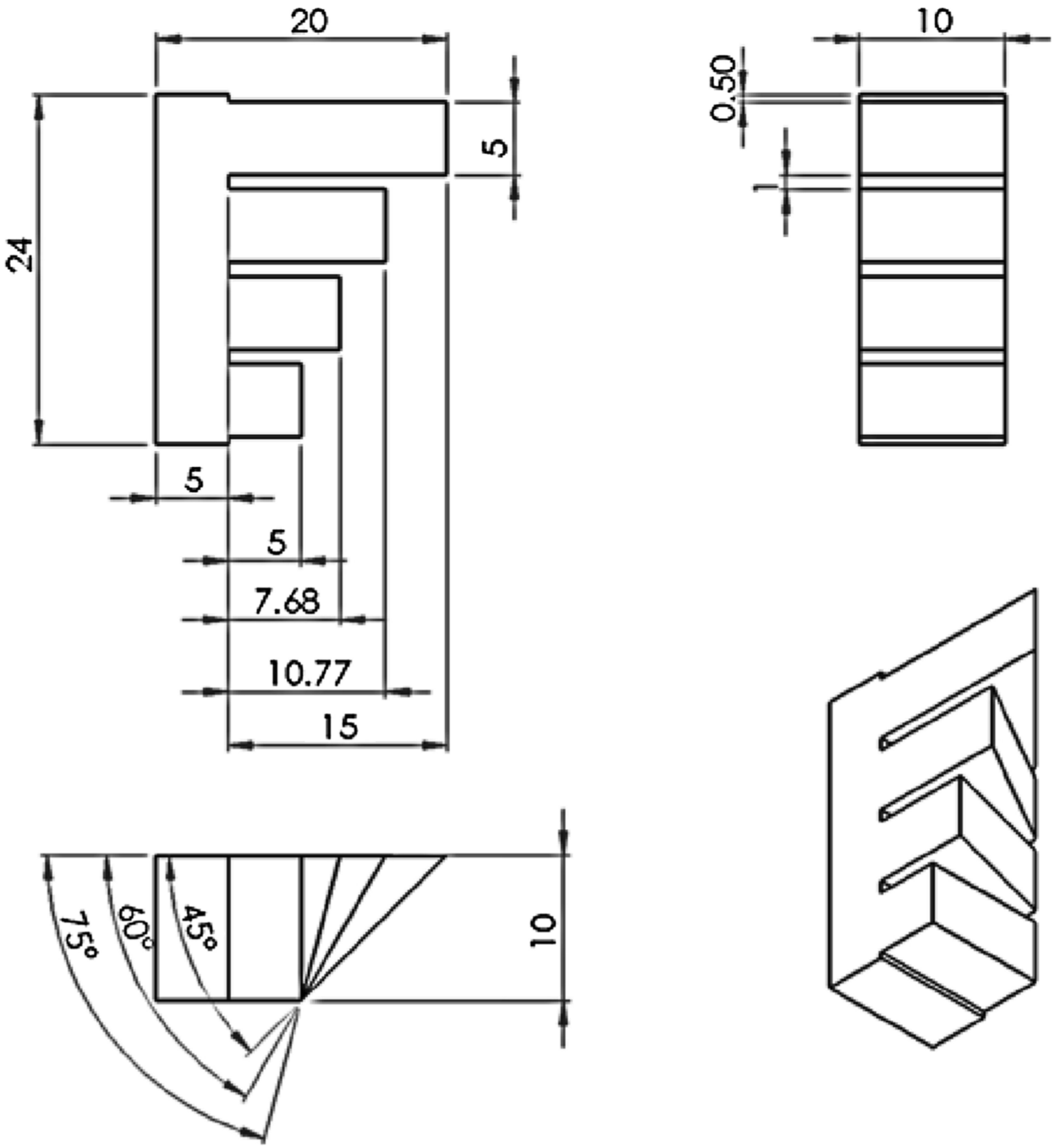

Fig. 6.

Test part design. The part has four connected overhanging wedges with width 5 mm, height 10 mm and angles of 45, 60, 75, and 90 degrees respectively. Dimensions are in millimeters.

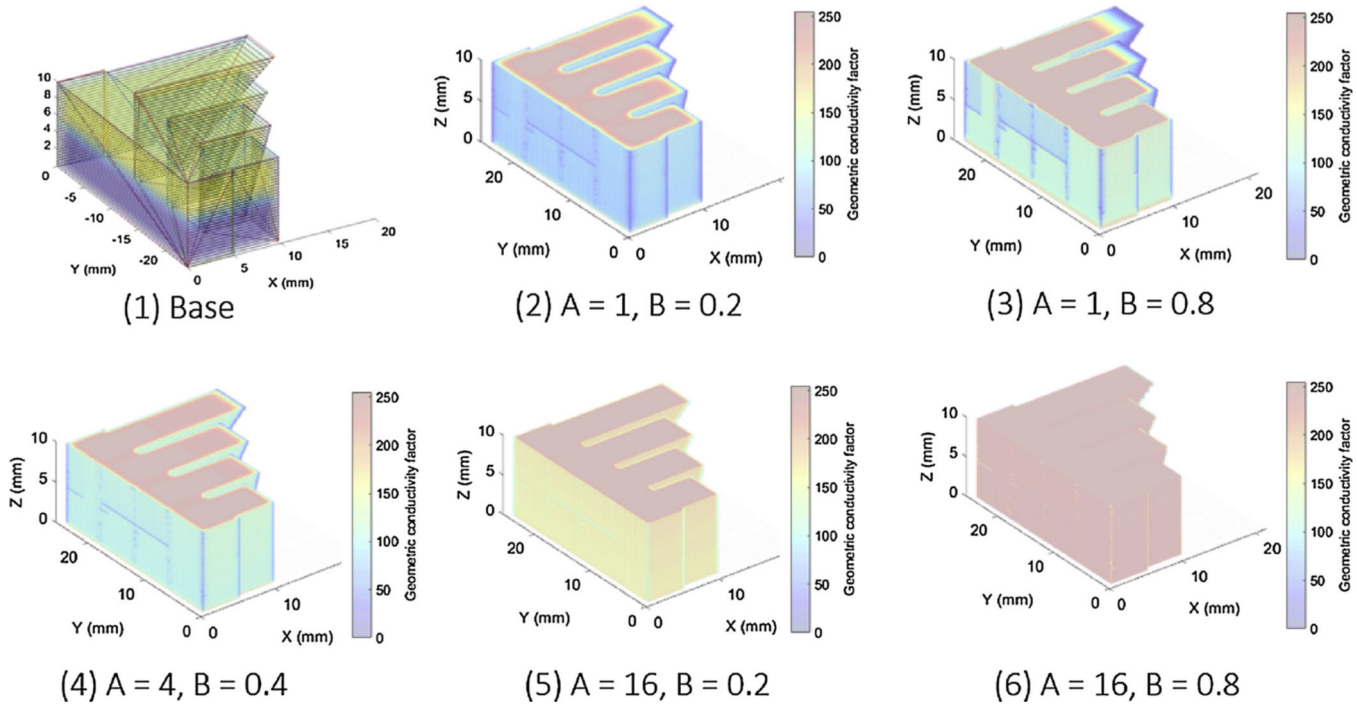

Fig. 7.

GCF models created by different A and B values. (1) is an STL plot of the original structure to represent the base.

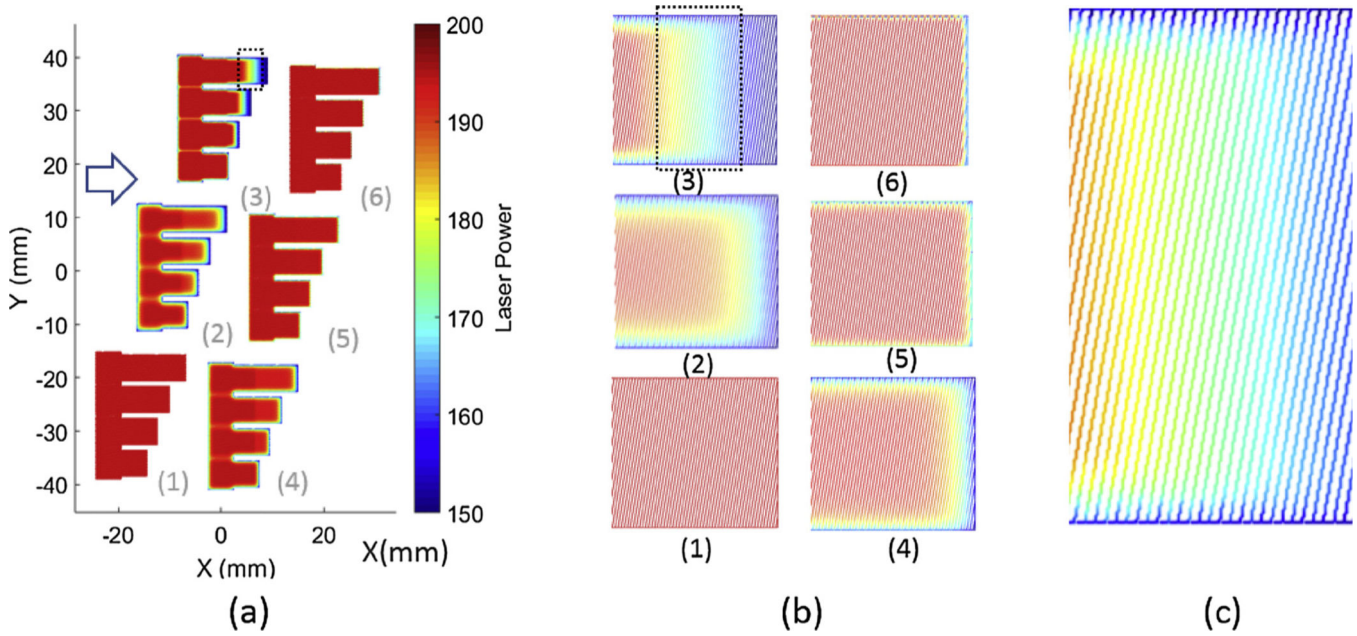

Fig. 8.

Laser path and power plots for layer 380. (a) Layout of the six parts, arrow indicates the recoating direction. (b) Expanded view of the 45o overhangs. (c) Expanded view of part 3 to show the power variation. The dotted line rectangle indicated the location of (c) in (a) and (b).

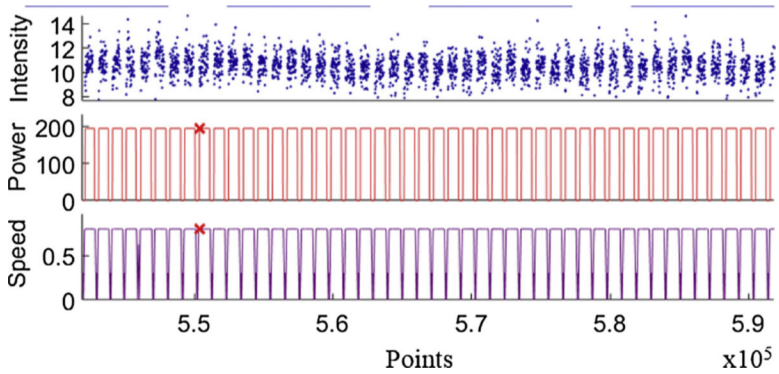

Fig. 9.

In-situ melt-pool images intensity for layer 415 over the 45o overhang of part 1. The melt-pool image intensity is plotted together with the laser power and speed.

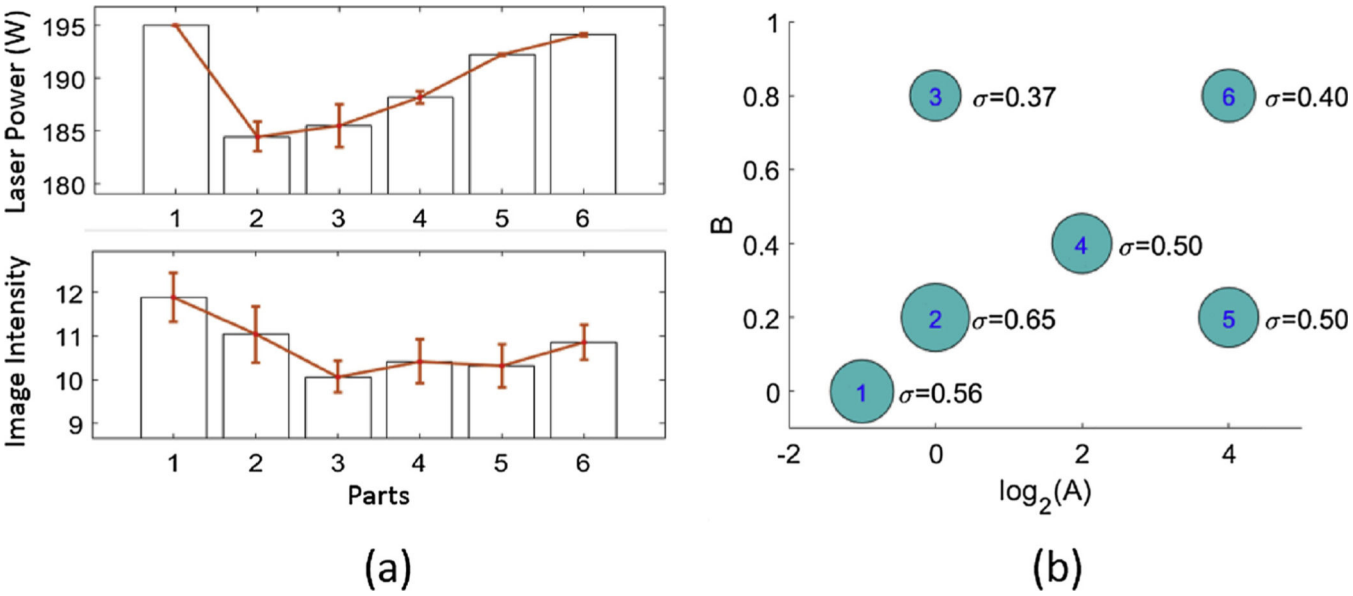

Fig. 10.

(a) Top shows average laser power for each part, bottom shows average melt-pool image intensity. The 'error' bars represent one standard deviation. (b) Standard deviation of melt-pool image intensity (represented as circle radii) vs. A and B parameters of the GCF model.

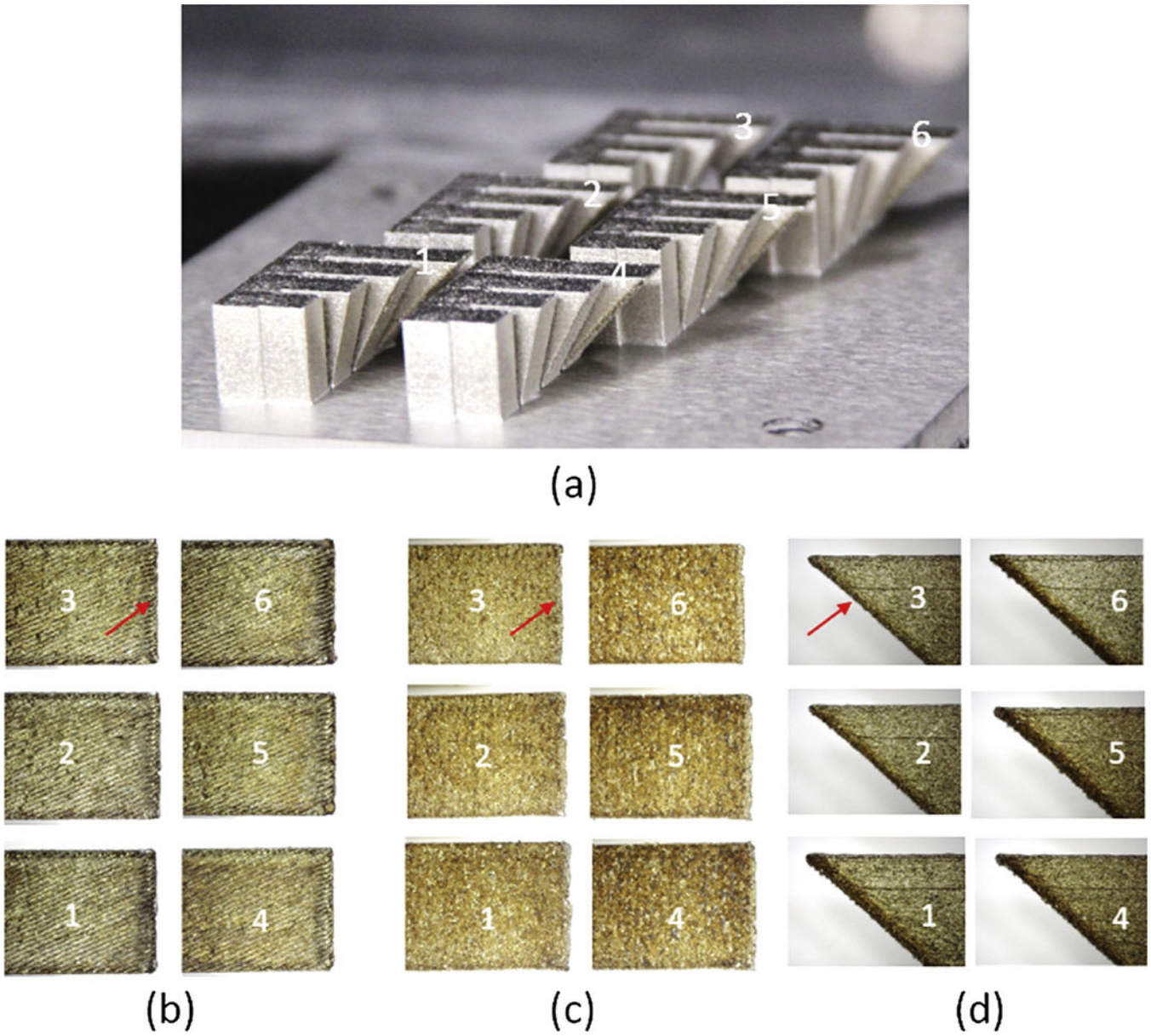

Fig. 11.

(a) six parts attached to the base plate as built, (b) – (d) are upward-facing, downward-facing, and side-facing surfaces of the 45o overhangs. (For interpretation of the references to colour in this figure text, the reader is referred to the web version of this article).

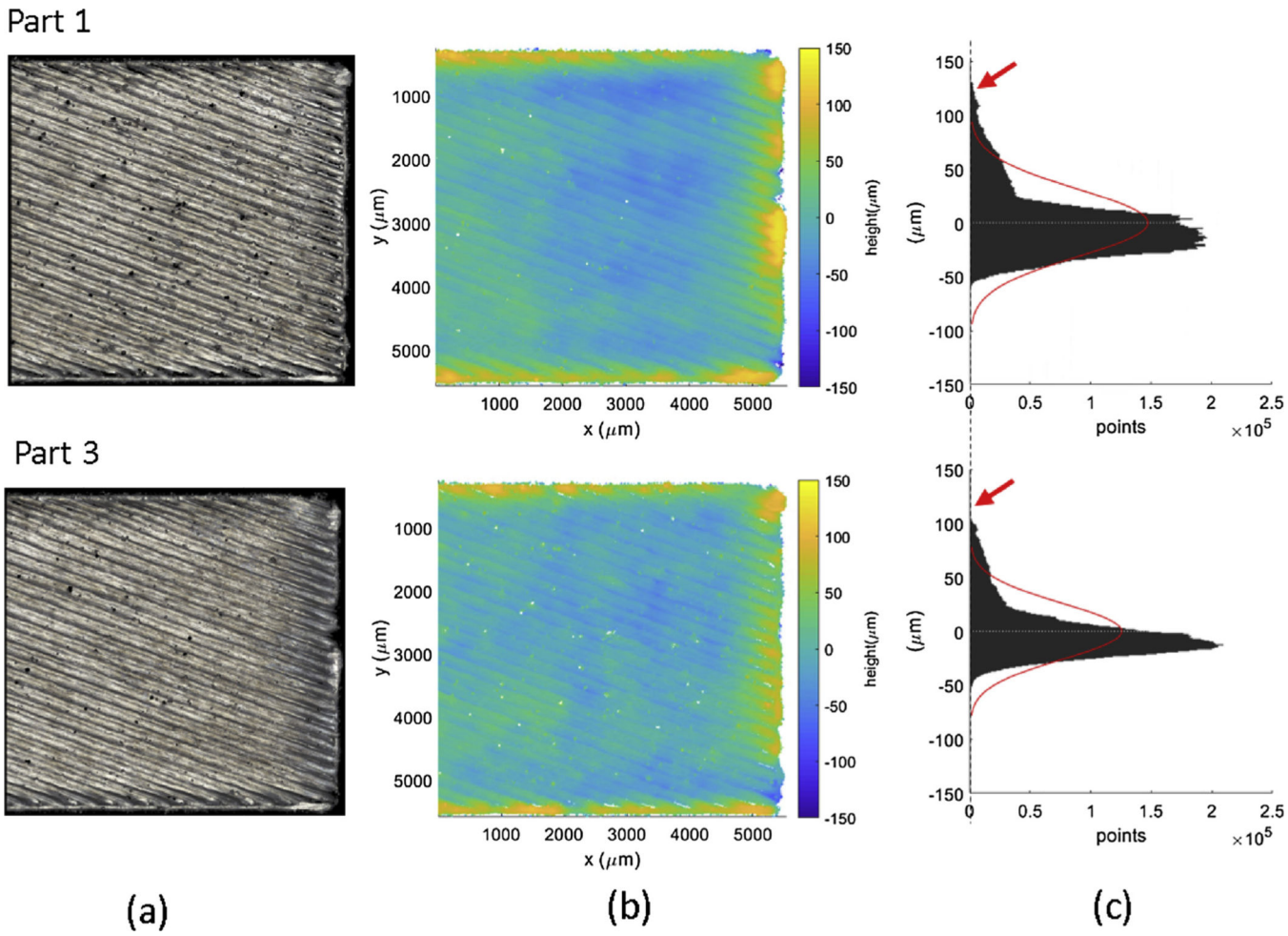

Fig. 12.

For parts 1 and 3: (a) True-color image of the faceup surface, (b) false-color height map of the upward-facing surface, and (c) histogram of height values. (For interpretation of the references to colour in this figure text, the reader is referred to the web version of this article).

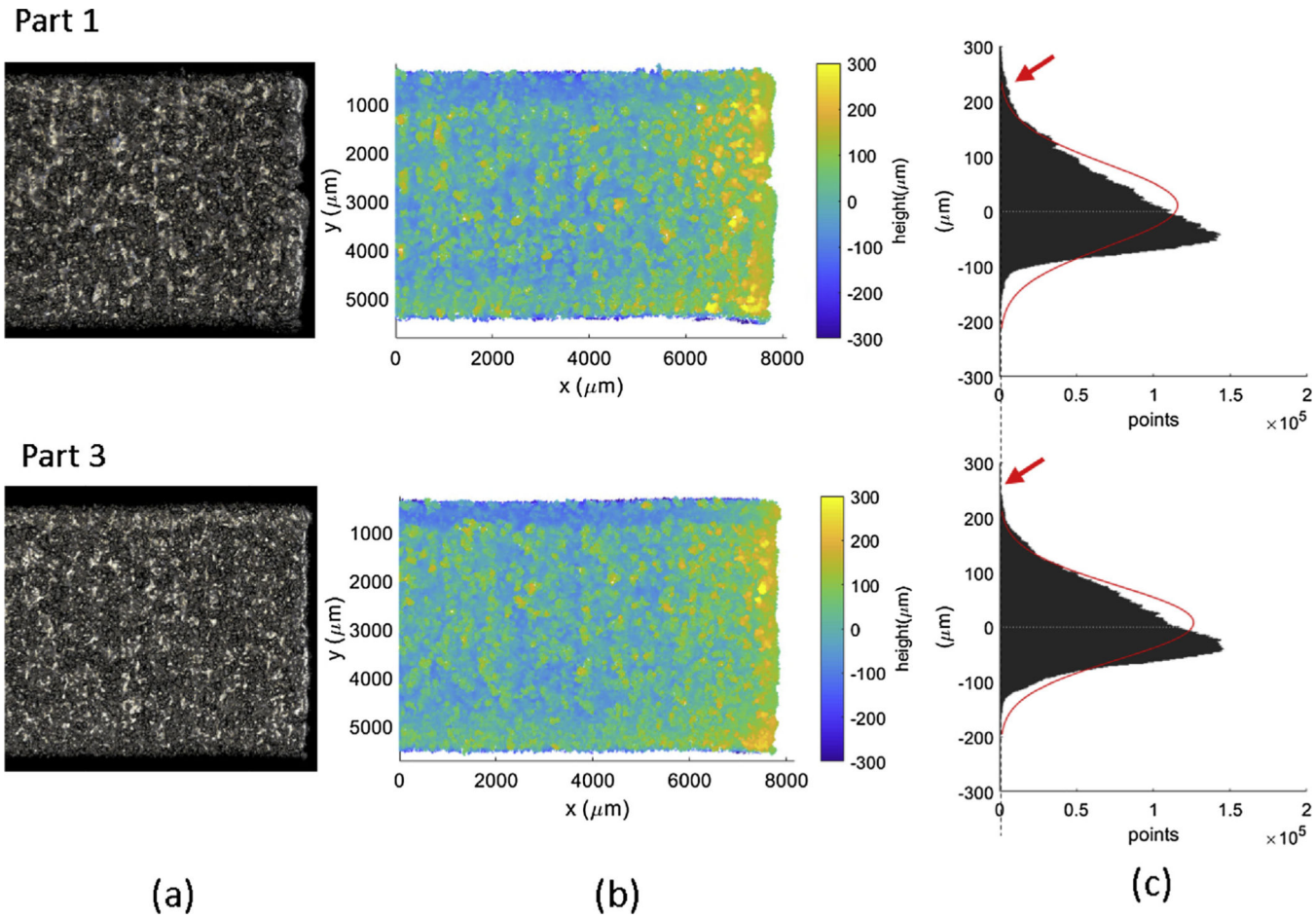

Fig. 13.

For parts 1 and 3: (a) True-color image of the facedown surface, (b) false-color height map of the downward-facing surface, and (c) histogram of height values. (For interpretation of the references to colour in this figure text, the reader is referred to the web version of this article).

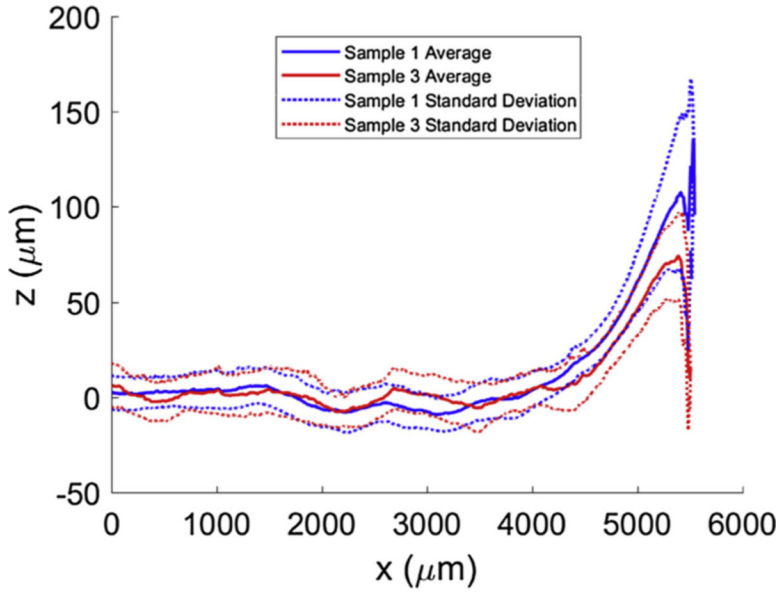

Fig. 14.

Average height for values y such that 0 μm ≤ y ≤ 5000 μm at various positions along x for the upward-facing surfaces of part 1 and part 3.

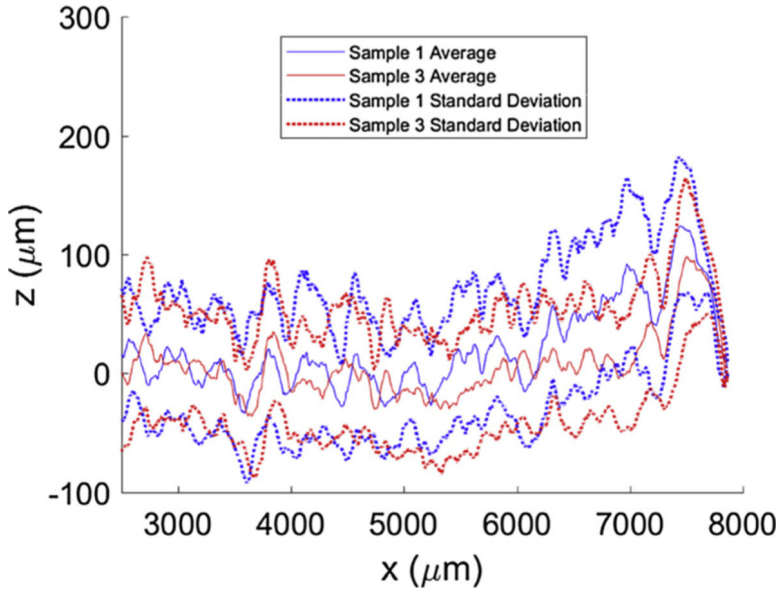

Fig. 15.

Average height along the y-direction at various positions along x for the downward-facing surfaces of part 1 and part 3.

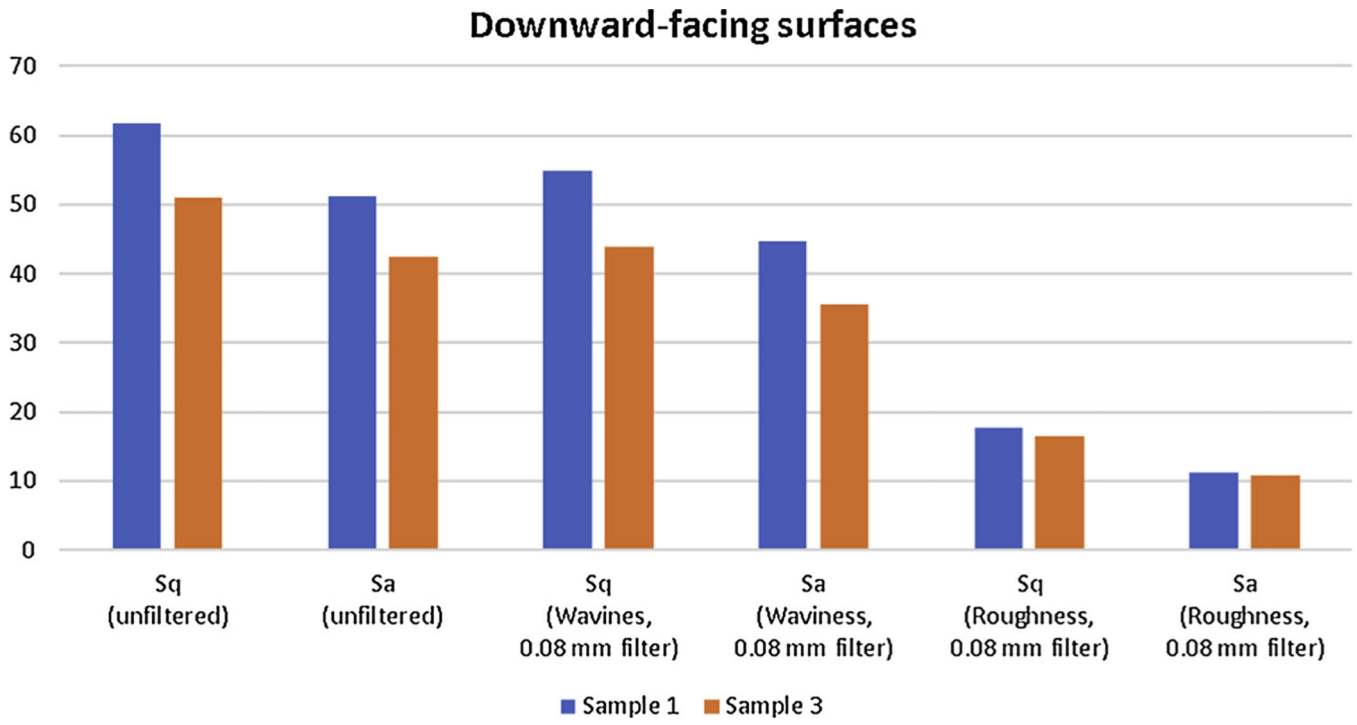

Fig. 16.

Surface roughness comparison for part 1 and part 3. Filter used is a digital gaussian filter with cutoff wavelength of 0.08 mm.

Table 1

GCF values update.

GCF \ Scan points	P1	P2	P3	P4	P5
Dynamic GCF	*208.00*	*213.33*	*213.46*	*219.07*	*230.32*
t1	*208.00*	-	-	-	-
t2	213.33	*213.33*	-	-	-
t3	213.33	218.67	*213.46*	-	-
t4	213.33	224.15	218.94	*219.07*	-
t5	219.09	229.91	224.70	224.84	*230.32*
Static GCF	219.09	229.91	224.70	224.84	230.32

Table 2

Characteristics for high-speed co-axial melt pool monitoring system.

Pixel Pitch of Detector	**8 μm**
Window Size (H x V)	120 × 120 pixels
Instantaneous Field of View	8 μm/pixel
Magnification	1x
Frame Rate	< 10 000 frames/s
Shutter Speed	20 μs
Bit depth	8-bit (256 digital levels)
Optical Filter Bandwidth	850 nm ± 20 nm